



Voltage-modulated magnetic properties and enhanced thermal endurance in Ta/Mo-based perpendicular magnetic tunnel junctions

S. Wu , G.J. Lim, F.N. Tan, T.L. Jin, C.C.I. Ang, K.J. Cheng, W.S. Lew ^{*}

School of Physical and Mathematical Sciences, Nanyang Technological University, 21 Nanyang Link, Singapore 637371 Singapore

ABSTRACT

In this work, we experimentally demonstrate Ta/Mo-based perpendicular magnetic tunnel junctions (pMTJs) with a double CoFeB free layer, engineered to leverage the complementary properties of the strong spin-orbit coupling of Ta and the interfacial anisotropy enhancement of Mo. The Ta/Mo bilayer significantly improves interfacial stability, perpendicular magnetic anisotropy (PMA) and thermal endurance, allowing the device to sustain PMA up to 550 °C, surpassing the thermal limits of conventional Ta-based structures. Furthermore, the application of gate voltage enables efficient modulation of the anisotropy field and coercivity, leading to a 23% reduction in switching current, demonstrating the efficacy of voltage-controlled magnetic anisotropy (VCMA) in lowering the energy barrier for magnetization reversal. This synergistic combination of spin-orbit torque (SOT) and VCMA mechanisms highlights the potential of the optimized Ta/Mo system for energy-efficient, high-performance memory and logic applications with low power consumption under elevated thermal conditions.

1. Introduction

Perpendicular magnetic tunnel junctions (pMTJs) with voltage-controlled magnetic anisotropy (VCMA) and spin-orbit torque (SOT) have emerged as critical building blocks for next-generation high-performance, energy-efficient, and scalable non-volatile memory technologies, particularly in spin-orbit torque magnetic random-access memory (SOT-MRAM) [1–7]. The ability to manipulate perpendicular magnetic anisotropy (PMA) via an external electric field provides an alternative to current-driven magnetization switching, significantly reducing power consumption and enabling ultra-low-energy operation [8–13]. In conventional pMTJs, CoFeB/MgO interfaces provide strong interfacial PMA, making them the preferred choice for high-performance magnetoresistive random-access memory (MRAM) applications. However, Ta/CoFeB/MgO-based stacks suffer from interfacial PMA degradation above 400 °C, limiting their thermal endurance and compatibility with complementary metal-oxide-semiconductor (CMOS) processes. Additionally, the VCMA effect in Ta-based structures remains suboptimal due to weak modulation of interfacial anisotropy and limited charge accumulation at the Ta/CoFeB/MgO interface, mainly caused by interfacial roughness, atomic intermixing and reduced dielectric response under electric fields [14–19]. To address these limitations, alternative buffer and capping layers such as Hf, W, and Mo have been explored [20]. W-based stacks have demonstrated improved thermal endurance and SOT efficiency [21–24]. In particular, Mo has garnered significant attention due to its unique ability to enhance interfacial PMA and improve

thermal endurance without compromising the spin polarization and tunnel magnetoresistance (TMR) of the MTJ [25]. Mo-based CoFeB/MgO stacks have demonstrated superior performance, including sustained PMA and enhanced interfacial anisotropy at high annealing temperatures, exceeding the thermal tolerance of Ta-based counterparts [26–28]. This enhancement is attributed to the higher crystallinity, reduced interfacial intermixing, and thermal robustness of Mo [27,29]. Furthermore, the integration of ultrathin Mo spacer layers into MgO/CoFeB/Mo/CoFeB/MgO junctions has been shown to yield PMA values exceeding 0.3 mJ/m², with promising VCMA effects that enable energy-efficient magnetization switching [26]. Complementary studies on Mo-based multilayers, such as CoMn/Mo/CoFeB structures, have also demonstrated robust perpendicular anisotropy and tunneling magnetoresistance exceeding 100% [30]. While Mo exhibits weaker spin-orbit coupling compared to heavy metals like Ta or W, recent studies have highlighted its potential as an efficient spin current generator in SOT-based systems. The field-like and damping-like torques generated in Mo/CoFeB/MgO heterostructures are sufficient for achieving current-induced magnetization switching [25,31,32].

In this work, we systematically investigate the (Ta/Mo)₅-based pMTJ system, leveraging the synergistic properties of Ta and Mo to optimize SOT efficiency, thermal endurance and VCMA response. By tuning the Ta/Mo bilayer thickness and incorporating a Mo spacer within a double CoFeB free layer, we achieve a multilayer structure optimized for enhanced perpendicular anisotropy and voltage-controlled magnetization switching. To evaluate thermal endurance, an investigation across

^{*} Corresponding author.

E-mail address: wensiang@ntu.edu.sg (W.S. Lew).

<https://doi.org/10.1016/j.jmmm.2025.173293>

Received 15 April 2025; Received in revised form 3 June 2025; Accepted 11 June 2025

Available online 13 June 2025

0304-8853/© 2025 Elsevier B.V. All rights reserved, including those for text and data mining, AI training, and similar technologies.

different annealing temperatures (450 °C, 500 °C, and 550 °C) is conducted, revealing that Mo-containing devices maintain robust PMA up to 550 °C, whereas Ta-based counterparts experience significant degradation. Furthermore, the application of a gate voltage enables efficient modulation of the anisotropy field, leading to a substantial 23% reduction in the switching current, thereby lowering the power required for magnetization reversal. With demonstrated thermal endurance, enhanced VCMA response and reduced switching current, the Ta/Mo-based pMTJ system is positioned as an energy-efficient, and thermally stable platform for next-generation magnetic memory and logic applications.

2. Experimental methods

Film Growth: The pMTJ stacks, consisting of [Ta (1.8 nm)/Mo (0.2 nm)]₅/CoFeB (1 nm)/Mo (0.4 nm)/CoFeB (1 nm)/MgO (1.5 nm)/CoFeB (1.2 nm)/Ta (5 nm), were fabricated on thermally oxidized Si substrates using magnetron sputtering at room temperature under an ultrahigh vacuum with a base pressure of 5×10^{-8} Torr. For SOT measurements, Hall bar devices based on simplified stacks without the top reference layer were also fabricated, using a structure of (Ta/Mo)₅/CoFeB/Mo/CoFeB/MgO/Ta. The use of two distinct structures for different characterization purposes is explicitly stated for clarity.

Device Fabrication: The fabrication of Ta/Mo-based pMTJ devices was carried out through a series of photolithography, electron-beam lithography (EBL), and Ar ion milling processes. Initially, AR-N4340 negative-tone resist was utilized to pattern the Ta/Mo underlayer, after which all layers were etched using Ar ion milling, and subsequent removal of the photoresist with acetone. MTJ pillars with circular geometries and diameters of 10 μm were then patterned by EBL with ma-N

2403 negative-tone resist, and etched down to the MgO layer. A 50 nm-thick HfO_x insulating layer was sputtered to electrically isolate the top and bottom contacts of the tunnel junctions. The top electrodes were patterned through a photolithography step using AZ5214 positive-tone resist, followed by the deposition of a 30 nm-thick Ta layer. A second photolithography and Ar ion milling process was employed to define and open the bottom electrodes, followed by the sputtering of an additional 30 nm-thick Ta layer. Finally, the fully patterned MTJ devices were annealed at 400 °C for 30 min under vacuum conditions.

Magnetic and Electrical Characterization: The magnetic properties of the thin films were evaluated using a vibrating sample magnetometer (VSM). For the Hall bar devices, the magnetic properties were characterized through electrical measurements via the anomalous Hall effect (AHE). The SOT efficiency was determined by measuring harmonic Hall voltages, utilizing a Keithley 6221 AC current source in conjunction with a 7265 Dual-Phase DSP Lock-In Amplifier [33]. The SOT switching behavior in the 3-terminal Ta/Mo-based pMTJ devices was measured by applying current and recording resistance using a Keithley 2400 source meter, while a bias magnetic field was provided by a LakeShore electromagnet. All measurements were conducted at room temperature.

3. Results and discussion

The structure illustrated in Fig. 1(a) represents the (Ta/Mo)₅/CoFeB/Mo/CoFeB/MgO/Ta thin film stack, where the bottom Ta/Mo bilayer configuration consists of alternating Ta and Mo layers with varying thicknesses, ranging from (Ta 1.8 nm/Mo 0.2 nm)₅ to (Ta 1.2 nm/Mo 0.8 nm)₅. The subscript “5” denotes the number of bilayer repetitions. Magnetic hysteresis loops recorded under an out-of-plane magnetic field (H_z) demonstrate robust PMA across all samples. Fig. 1(b) illustrates the

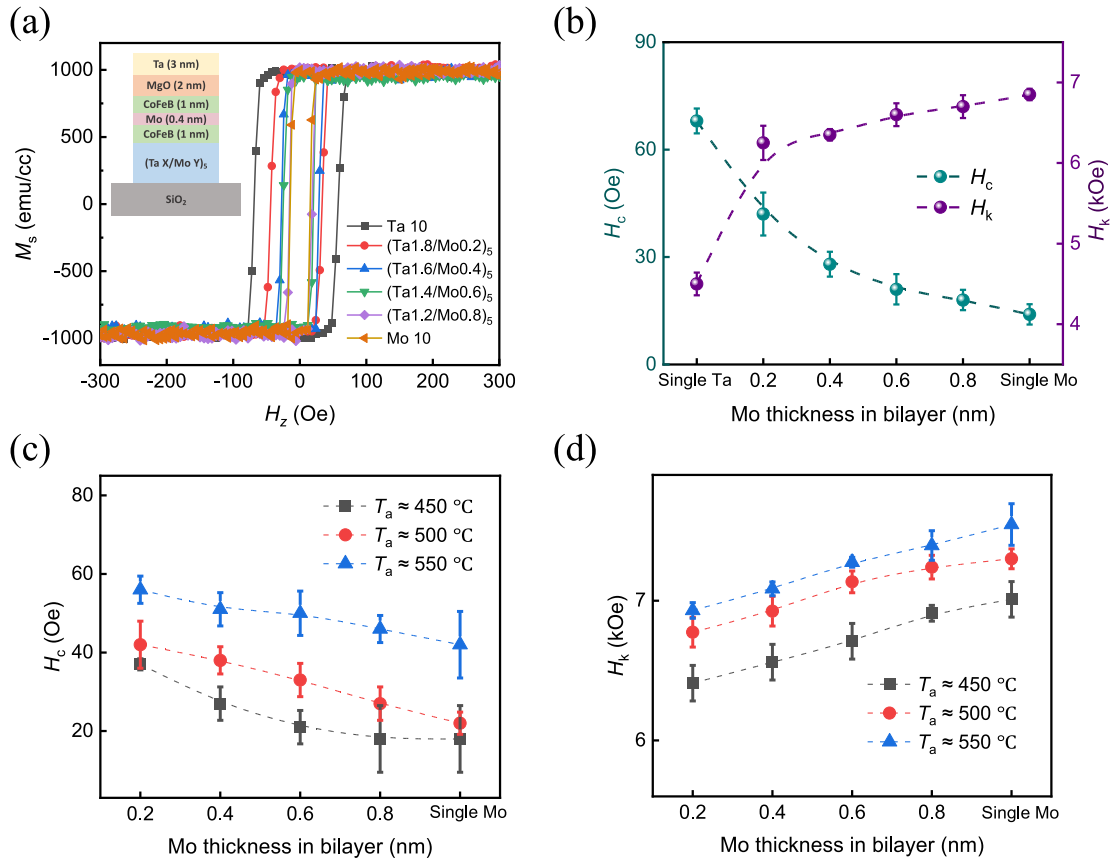


Fig 1. (a) Out-of-plane hysteresis loops of (Ta/Mo)₅/CoFeB/Mo/CoFeB/MgO/Ta films after annealing at 400 °C, along with a schematic illustration of the film structure. (b) Dependence of coercivity (H_c) and anisotropy field (H_k) on Mo thickness in the Ta/Mo bilayer after 400 °C annealing. (c) Variation of H_c and (d) H_k for different Ta/Mo films as a function of annealing temperature (T_a).

dependence of coercivity (H_c) and anisotropy field (H_k) on the Mo thickness within the Ta/Mo bilayer. A clear trend is observed, where H_c decreases with increasing Mo thickness, ranging from 68 Oe for the single-Ta-layer sample to 18 Oe for the sample with a thicker Mo thickness. The single-Mo-layer sample exhibits the lowest H_c , highlighting the influence of interfacial properties associated with Mo on the magnetization reversal process [31]. Conversely, H_k exhibits an increase with increasing Mo thickness, indicating enhanced perpendicular anisotropy. This is consistent with previous studies that have shown Mo to enhance interfacial anisotropy by promoting 3d–4d orbital hybridization at the CoFeB/MgO interface. This is consistent with previous studies that have shown Mo to enhance interfacial anisotropy by promoting 3d–4d orbital hybridization at the CoFeB/MgO interface. First-principles calculations further confirm that Mo insertion increases the magnetic anisotropy energy through stronger interfacial hybridization and spin–orbit coupling, compared to W, resulting in enhanced perpendicular anisotropy [27]. The improvement in PMA can be attributed to the role of Mo in modifying the electronic structure at the $\text{Co}_{40}\text{Fe}_{40}\text{B}_{20}$ interface, which enhances spin–orbit coupling and strengthens the perpendicular anisotropic energy barrier [29]. To further investigate the thermal endurance of the Ta/Mo bilayer structure, samples were annealed at $T_a \approx 450, 500, \text{ and } 550^\circ\text{C}$, revealing that all Mo-containing samples retained PMA at elevated temperatures, whereas the single-Ta-layer sample lost PMA entirely (the magnetic hysteresis loops are included in [Supplementary Material S1](#)). This result demonstrates the excellent thermal endurance of the selected multilayer design, which surpasses that of conventional structures typically composed of Ta/CoFeB-based systems, where PMA degradation is often reported at lower annealing thresholds due to interfacial diffusion and magnetic layer deterioration. First-principles calculations have shown that Mo-based stacks exhibit reduced interfacial reactivity and enhanced interfacial orbital hybridization, leading to improved thermal robustness [27]. Experimental studies further confirm that Mo insertion suppresses B diffusion and preserves PMA after high-temperature annealing [34,35]. [Fig. 1\(c\)](#) and [\(d\)](#) further illustrate the evolution of H_c and H_k with Mo thickness under different annealing conditions. As shown in [Fig. 1\(c\)](#), H_c decreases with increasing Mo thickness across all annealing temperatures. At each fixed Mo thickness, H_c increases with T_a . In contrast, [Fig. 1\(d\)](#) shows that H_k increases monotonically with Mo thickness at all annealing temperatures, indicating enhanced PMA stabilization through Mo-mediated interfacial hybridization effects. Additionally, higher T_a results in an overall increase in H_k , suggesting that annealing facilitates improved crystallization by enabling the transformation of initially amorphous CoFeB into a bcc (001) textured phase, as a result of increased atomic mobility at elevated temperatures. This crystallization reinforces interfacial anisotropy, contributing to the

observed enhancement in magnetic properties [36]. Mo's unique ability to increase interfacial anisotropy energy stems from its electronic structure, which facilitates strong hybridization at the CoFeB/Mo interface [27]. Moreover, this enhancement can be attributed to the minimal intermixing at the CoFe/Mo interface [26]. The $(\text{Ta}/\text{Mo})_5$ bilayer amplifies these effects by creating a composite structure where the contribution of each interface becomes cumulative. This configuration provides a platform for tailoring magnetic properties by balancing the strong spin–orbit coupling from Ta with the anisotropic enhancements offered by Mo. The observed trend in H_c and H_k underscores the pivotal role of Mo in Ta/Mo bilayers for maintaining PMA and optimizing thermal endurance in CoFeB-based heterostructures.

Subsequently, the $(\text{Ta}/\text{Mo})_5/\text{CoFeB}/\text{Mo}/\text{CoFeB}/\text{MgO}/\text{Ta}$ thin films were fabricated into $10\ \mu\text{m} \times 100\ \mu\text{m}$ Hall cross devices. Consistent with the hysteresis behavior of the thin films, the anomalous Hall resistance ($R_{\text{AHE}}-H_z$) loops shown in [Fig. 2\(a\)](#) reveal that devices with thicker Mo layers exhibit reduced coercivity compared to devices with thinner Mo layers. To quantify the damping-like torque efficiency χ_{DL} as a function of Ta/Mo bilayer thickness, first-harmonic ($V_{1\omega}$) and second-harmonic ($V_{2\omega}$) Hall voltage measurements were performed under in-plane magnetic fields applied along the current (x-direction) and transverse (y-direction) directions (the first- and second-harmonic Hall voltage measurement plots are included in [Supplementary Material S2](#)). The damping-like torque efficiency was calculated using the relation: [33]

$$\chi_{\text{DL}} = \frac{2e}{\hbar} \cdot \frac{M_s t_{\text{FM}} H_{\text{DL}}}{J}$$

where M_s is the saturation magnetization, t_{FM} is the ferromagnetic layer thickness, H_{DL} is the extracted damping-like effective field, and J is the applied current density. The results, shown in [Fig. 2\(b\)](#), indicate that χ_{DL} decreases with increasing Mo layer thickness. The inset shows the optical micrograph of the Hall bar structure. While Mo is recognized for its excellent thermal endurance and significant contribution to PMA, its SOT efficiency is inherently lower than that of heavy metals like Ta [25]. However, in the $(\text{Ta } 1.8\ \text{nm}/\text{Mo } 0.2\ \text{nm})_5$ sample, the χ_{DL} is comparable to that of the single-Ta-layer sample. This indicates that this combination of Ta and Mo optimally balances their respective contributions, leveraging the strong spin–orbit coupling of Ta and the ability of Ta to enhance interfacial anisotropy and thermal endurance. Therefore, this combination is selected for subsequent studies. The choice of Ta 1.8 nm and Mo 0.2 nm thicknesses optimizes the balance between Ta's strong spin–orbit coupling and Mo's thermal endurance. The thermal endurance of this system reflects the benefits of carefully engineered interfacial interactions and bilayer thicknesses, providing a way for advancements in magnetic memory and logic applications requiring operation at elevated temperatures.

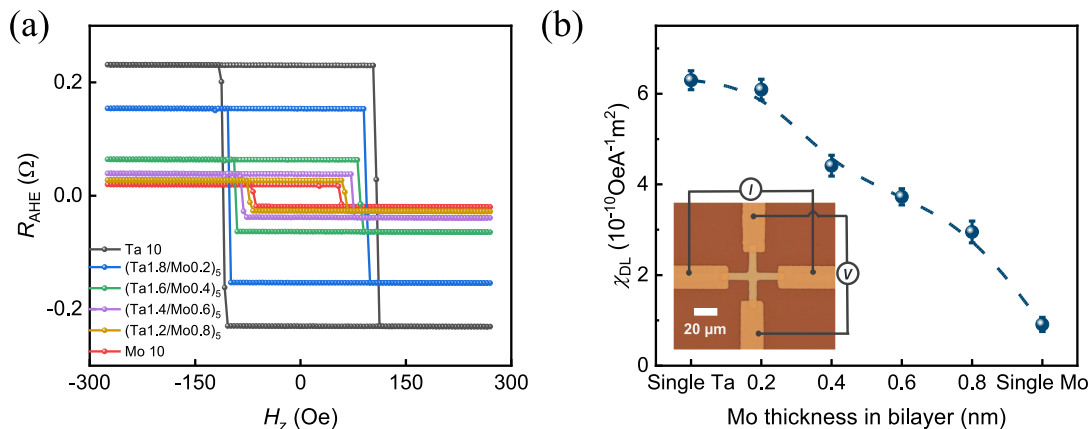


Fig. 2. (a) Anomalous Hall resistance loops measured on the Ta/Mo devices under an out-of-plane field. (b) The damping-like field SOT efficiency χ_{DL} dependence on the Ta/Mo thicknesses. The inset shows an optical micrograph of the Hall bar device. I is the applied current into the Hall cross. V is the measured Hall voltage.

Mo has a critical role in enhancing PMA through interfacial effects, and its sensitivity to electric fields makes it a promising material for voltage-controlled magnetic anisotropy (VCMA) [37]. To further investigate the VCMA effect and the role of Mo in enhancing perpendicular magnetic PMA, voltage-gated Hall devices were fabricated based on the $(\text{Ta } 1.8 \text{ nm}/\text{Mo } 0.2 \text{ nm})_5$ multilayer stack, as schematically illustrated in Fig. 3(a). The device configuration consists of a Hall cross structure with a 50 nm HfO_x dielectric layer deposited atop the magnetic multilayer, followed by a Ti (10 nm)/Cu (50 nm)/Ti (10 nm) gate electrode. A gate voltage (V_{gate}) ranging from -4 V to $+4 \text{ V}$ was applied to induce an electric field across the stack, enabling dynamic modulation of PMA via the VCMA effect. Fig. 3(b) presents the dependence of H_k on V_{gate} for both the $(\text{Ta}/\text{Mo})_5$ -based and Ta-based devices. H_k was determined from the parabolic fitting of normalized Hall resistance (R_{H}^{N}) as a function of the in-plane magnetic field (H_x), calculated using a second-order Maclaurin expansion (details available in Supplementary Material S3) [38]. The results demonstrate that H_k increases monotonically with increasing V_{gate} , indicating a field-induced enhancement of PMA in both systems. However, the Mo-containing device exhibits a significantly larger modulation of H_k compared to the Ta-based counterpart, suggesting that Mo enhances the VCMA response. This pronounced voltage sensitivity in the $(\text{Ta}/\text{Mo})_5$ -based structure can be attributed to the Rashba-type interfacial spin-orbit coupling at the Mo/CoFeB and CoFeB/MgO interfaces. Such coupling originates from structural inversion asymmetry and leads to non-equilibrium spin accumulation that generates spin-orbit torques [39]. Experimental reports of dominant field-like torque in Mo/CoFeB/MgO heterostructures support the presence of strong interfacial spin-orbit effects in similar systems [31]. The presence of Mo modifies the interfacial electronic structure, increasing the efficiency of charge redistribution under the applied electric field, thereby leading to a greater change in H_k [40,41]. Furthermore, Fig. 3(c) shows the dependence of coercivity H_c on gate voltage V_{gate} for both $(\text{Ta}/\text{Mo})_5$ -based and Ta-based devices, with H_c values extracted from the

anomalous Hall resistance (R_{AHE}) loops (see Supplementary Material S4 for full loops). The $(\text{Ta}/\text{Mo})_5$ -based device exhibits a significant dependence of H_c on V_{gate} , with H_c decreasing by approximately 21% from 86 Oe to 68 Oe as V_{gate} decreases from 0 V to -4 V . Conversely, H_c increases by approximately 19%, from 86 Oe to 106 Oe, when V_{gate} increases from 0 V to $+4 \text{ V}$. This pronounced tunability of H_c with V_{gate} highlights the strong VCMA effect in the $(\text{Ta}/\text{Mo})_5$ -based structure. The presence of Mo is known to influence interfacial orbital hybridization and spin-orbit coupling at the CoFeB/MgO interface, leading to a more efficient redistribution of interfacial charge under applied electric fields and thereby amplifying the VCMA response [28]. In contrast, the Ta-based device exhibits negligible variations in H_c across the same voltage range, indicating a much weaker VCMA effect. The minimal modulation of H_c suggests that Ta alone does not provide sufficient interfacial sensitivity to electric fields. This contrast between these devices confirms that Mo incorporation significantly enhances the voltage tunability of PMA, making it a promising material for energy-efficient, voltage-controlled spintronic applications.

The demonstrated tunability of H_c and H_k under applied electric fields underscores the potential of the $(\text{Ta}/\text{Mo})_5$ -based structure for applications in voltage-controlled magnetic tunnel junctions (VC-MTJs). The $(\text{Ta}/\text{Mo})_5$ -based structure exhibits significant promise due to its optimized design, which integrates a $(\text{Ta } 1.8/\text{Mo } 0.2)_5$ stack as the SOT channel, a double free layer consisting of two CoFeB layers separated by a 0.4 nm Mo spacer layer, a MgO tunneling barrier and a reference layer. Fig. 4(a) illustrates the schematic of this multilayer structure. The $(\text{Ta}/\text{Mo})_5$ stack provides a way for SOT generation while maintaining high thermal endurance and strong PMA. The optimized bilayer thicknesses of Ta and Mo balance the strong spin-orbit coupling from Ta with the interfacial anisotropy enhancement and thermal endurance contributed by Mo. During operation, current pulses applied to the $(\text{Ta}/\text{Mo})_5$ SOT channel induce magnetization switching in the double free layer through SOT. This design strategically leverages the complementary

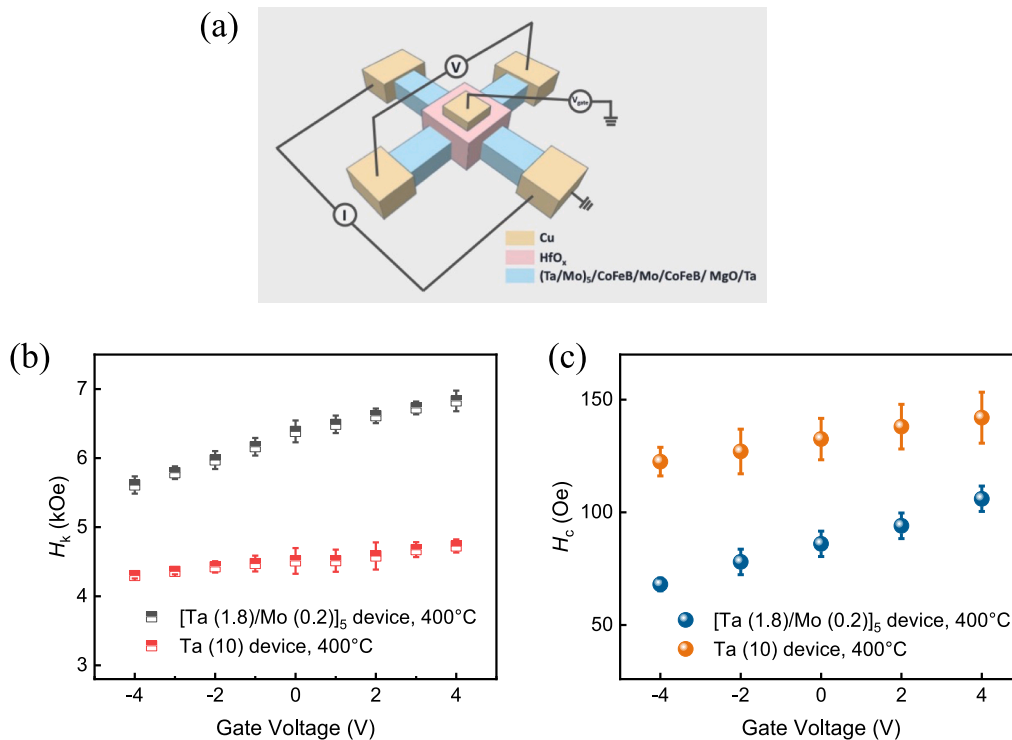


Fig. 3. (a) Schematic illustration of the voltage-controlled coupling and electrical measurement setup. I is the applied current into the Hall cross. V is the measured Hall voltage in the crossbar. V_{gate} is the applied gate voltage. Dependence of (b) magnetic anisotropy field (H_k) and (c) coercivity (H_c) on the gate voltage (V_{gate}) for $(\text{Ta } 1.8/\text{Mo } 0.2)_5$ and Ta (10) devices. The $(\text{Ta } 1.8/\text{Mo } 0.2)_5$ device consists of $(\text{Ta } 1.8/\text{Mo } 0.2)_5/\text{CoFeB } (1)/\text{Mo } (0.4)/\text{CoFeB } (1)/\text{MgO } (2)/\text{Ta } (3)$, while the Ta device uses a Ta (10) underlayer with an identical upper stack. All devices were annealed at $400 \text{ }^\circ\text{C}$. All thicknesses in parentheses are in nanometers.

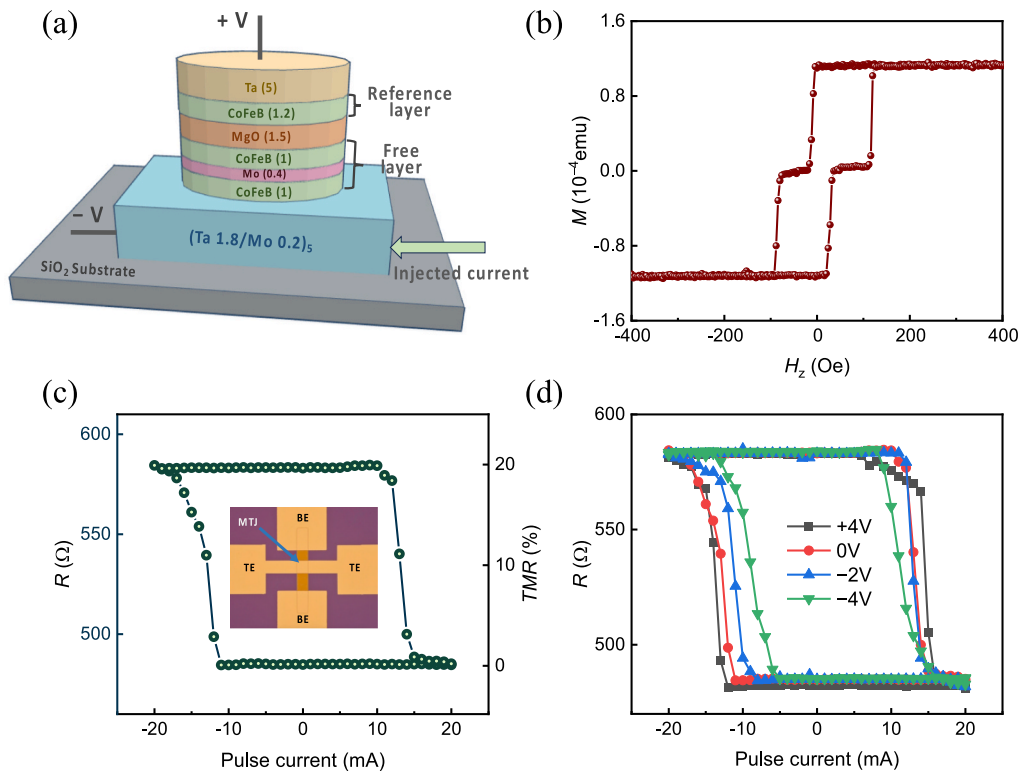


Fig 4. (a) Schematic of the Ta/Mo-based perpendicular magnetic tunnel junction (pMTJ) with double free layers. (b) Out-of-plane magnetic hysteresis loops of the Ta/Mo-based MTJ film. (c) Current-induced magnetization switching in the Ta/Mo-based pMTJ device. The inset shows the optical micrograph of the patterned MTJ device with a diameter of $5 \mu\text{m}$. (d) Voltage-controlled current-induced magnetization switching in the Ta/Mo-based pMTJ device under $V_{\text{gate}} = -4 \text{ V}, -2 \text{ V}, 0 \text{ V}$ and $+4 \text{ V}$.

properties of Ta and Mo to achieve reliable switching with low energy consumption. The magnetic hysteresis loops of the Ta/Mo-based MTJ thin film stack, shown in Fig. 4(b), reveal the characteristic double-switching behavior associated with the independent magnetization reversal of the two CoFeB layers in the double free layer. The stack configuration, $[\text{Ta} (1.8 \text{ nm})/\text{Mo} (0.2 \text{ nm})]_5/\text{CoFeB} (1 \text{ nm})/\text{Mo} (0.4 \text{ nm})/\text{CoFeB} (1 \text{ nm})/\text{MgO} (1.5 \text{ nm})/\text{CoFeB} (1.2 \text{ nm})/\text{Ta} (5 \text{ nm})$, is carefully engineered. The hysteresis loops confirm that the multilayer design effectively supports robust PMA. Fig. 4(c) demonstrates the current-induced SOT switching in the Ta/Mo-based pMTJ device, with the inset showing the optical micrograph of the patterned MTJ with a $5 \mu\text{m}$ diameter. During operation, 5 ms current pulses applied to the $(\text{Ta}/\text{Mo})_5$ SOT channel induce magnetization switching in the double free layer, with an in-plane magnetic field of 300 Oe applied to facilitate the process. The magnetization states of the MTJ device are subsequently read using a DC current of $100 \mu\text{A}$ between the top and bottom electrodes, with the TMR ratio measured at approximately 20%. Although Mo inherently exhibits lower spin-orbit torque efficiency than Ta, the optimized $(\text{Ta} 1.8/\text{Mo} 0.2)_5$ stack effectively enhances the overall device performance by combining Ta's strong spin-orbit coupling with Mo's ability to improve interfacial anisotropy. This synergy demonstrates the potential of this bilayer structure in enabling reliable magnetization switching with low power consumption. The voltage-controlled switching behavior is further analyzed in Fig. 4(d), which depicts the influence of V_{gate} on current-induced magnetization switching. By applying gate voltages ranging from -4 V to $+4 \text{ V}$ across the MTJ structure, the switching current is modulated, revealing a significant electric field effect on the magnetic properties of the device. At $V_{\text{gate}} = -4 \text{ V}$, the average switching current decreases by approximately 23%, from 13 mA at 0 V to 10 mA, indicating that the application of a negative voltage reduces the energy barrier for magnetization switching. This reduction can be attributed to the electric field-induced changes in

interfacial orbital hybridization and charge distribution at the CoFeB/Mo interface [41,42]. Conversely, a gate voltage of $+4 \text{ V}$ increases the switching current slightly beyond the baseline. The observed modulation of switching current demonstrates the potential of the $(\text{Ta}/\text{Mo})_5$ structure for voltage-tunable spintronic devices, where electric fields provide an additional degree of control over magnetization dynamics. The integration of an optimized $(\text{Ta}/\text{Mo})_5$ SOT channel and a double free layer design in the Ta/Mo-based VC-MTJ structure provides a robust platform for energy-efficient magnetic memory applications. The demonstrated voltage control of switching currents highlights the potential for reducing power consumption and enhancing device functionality through interfacial engineering and electric field modulation.

4. Conclusion

In conclusion, we experimentally demonstrated that Ta/Mo-based perpendicular magnetic tunnel junctions with a double CoFeB free layer exhibit enhanced thermal endurance, voltage-controlled magnetic anisotropy and SOT switching efficiency. The incorporation of Mo within the Ta/Mo bilayer significantly improves interfacial anisotropy and thermal robustness, enabling PMA to be maintained up to $550 \text{ }^\circ\text{C}$, exceeding the thermal endurance of conventional Ta-based structures. Hall resistance measurements further confirmed that the Mo-containing devices exhibit a stronger response to electric-field modulation, facilitating efficient voltage-controlled tuning of magnetic properties. Additionally, the application of gate voltage resulted in a 23% reduction in the switching current, demonstrating the effectiveness of VCMA in reducing the energy barrier for magnetization reversal. These results demonstrate the Ta/Mo-based system as a robust, energy-efficient, and scalable solution for next-generation spintronic devices, offering a practical pathway for memory and logic applications that demand low power consumption and high thermal endurance.

CRedit authorship contribution statement

S. Wu: Writing – original draft, Methodology, Investigation, Formal analysis, Data curation. **G.J. Lim:** Writing – review & editing, Methodology, Formal analysis, Conceptualization. **F.N. Tan:** Writing – review & editing, Validation, Methodology, Formal analysis. **T.L. Jin:** Writing – review & editing, Validation, Formal analysis, Conceptualization. **C.C.I. Ang:** Writing – review & editing, Formal analysis. **K.J. Cheng:** Investigation, Data curation. **W.S. Lew:** Writing – review & editing, Supervision, Conceptualization.

Declaration of competing interest

The authors declare that they have no known competing financial interests or personal relationships that could have appeared to influence the work reported in this paper.

Acknowledgment

This work was supported by MOE Tier 1 grant (No. RG76/23).

Appendix A. Supplementary data

Supplementary data to this article can be found online at <https://doi.org/10.1016/j.jmmm.2025.173293>.

Data availability

Data will be made available on request.

References

- [1] D.C. Worledge, G. Hu, D.W. Abraham, P.L. Trouilloud, S. Brown, J. Appl. Phys. 115 (2014) 172601.
- [2] Q. Shao, P. Li, L. Liu, H. Yang, S. Fukami, A. Razavi, H. Wu, K. Wang, F. Freimuth, Y. Mokrousov, M.D. Stiles, S. Emori, A. Hoffmann, J. Åkerman, K. Roy, J.-P. Wang, S.-H. Yang, K. Garello, W. Zhang, IEEE Trans. Magn. 57 (2021) 1.
- [3] B. Tudu, A. Tiwari, Vacuum 146 (2017) 329.
- [4] S. Ikegawa, F.B. Mancoff, S. Aggarwal, IEEE Int Interconnect Technol. Conf. 2021 (2021) 1–3.
- [5] M. Cubukcu, O. Boule, N. Mikuszzeit, C. Hamelin, T. Brächer, N. Lamard, M.-C. Cyrille, L. Buda-Prejbeanu, K. Garello, I.M. Miron, O. Klein, G. de Loubens, V. V. Naletov, J. Langer, B. Ocker, P. Gambardella, G. Gaudin, IEEE Trans. Magn. 54 (2018) 1.
- [6] B. Dieny, M. Chshiev, Rev. Mod. Phys. 89 (2017) 25008.
- [7] Spin Reflection-Induced Field-Free Magnetization Switching in Perpendicularly Magnetized MgO/Pt/Co Heterostructures Tianli Jin, Gerard Joseph Lim, Han Yin Poh, Shuo Wu, Funan Tan, and Wen Siang Lew ACS Applied Materials & Interfaces 2022 14 (7), 9781-9787.
- [8] S. Ikeda, K. Miura, H. Yamamoto, K. Mizunuma, H.D. Gan, M. Endo, S. Kanai, J. Hayakawa, F. Matsukura, H. Ohno, Nat. Mater. 9 (2010) 721.
- [9] S. Yakata, H. Kubota, Y. Suzuki, K. Yakushiji, A. Fukushima, S. Yuasa, K. Ando, J. Appl. Phys. 105 (2009) 07D131.
- [10] C. Song, B. Cui, F. Li, X. Zhou, F. Pan, Prog. Mater. Sci. 87 (2017) 33.
- [11] Shuo Wu, Tianli Jin, Calvin Ching Ian Ang, Gerard Joseph Lim, Bryan Wei Hao Cheng, Ze Chen and Wen Siang Lew 2024 Nanotechnology 35 365205.
- [12] F.N. Tan, G.J. Lim, T.L. Jin, H.X. Liu, F. Poh, W.S. Lew, Electric field control on single and double Pt/Co heterostructure for enhanced thermal stability, Journal of Magnetism and Magnetic Materials 490 (2019) 165448.
- [13] F.N. Tan, Q.Y. Wong, W.L. Gan, S.H. Li, H.X. Liu, F. Poh, W.S. Lew, Electric field control for energy efficient domain wall injection, Journal of Magnetism and Magnetic Materials, Volume 485, 2019, Pages 174–179, ISSN 0304-8853.
- [14] H. Meng, R. Shibiaa, C.C. Wang, S.Y.H. Lua, M.A.K. Akhtar, J. Appl. Phys. 110 (2011) 103915.
- [15] W.-G. Wang, S. Hageman, M. Li, S. Huang, X. Kou, X. Fan, J.Q. Xiao, C.L. Chien, Appl. Phys. Lett. 99 (2011) 102502.
- [16] H.D. Gan, H. Sato, M. Yamanouchi, S. Ikeda, K. Miura, R. Koizumi, F. Matsukura, H. Ohno, Appl. Phys. Lett. 99 (2011) 252507.
- [17] N. Miyakawa, D.C. Worledge, K. Kita, I.E.E.E. Magn. Lett 4 (2013) 1000104.
- [18] D.D. Awschalom, M.E. Flatté, Nat. Phys. 3 (2007) 153.
- [19] W.S. A., A.D. D., B.R. A., D.J. M., von M. S., R.M. L., C.A. Y., and T.D. M., Science (80-.). 294, 1488 (2001).
- [20] S. Peng, W. Zhao, J. Qiao, L. Su, J. Zhou, H. Yang, Q. Zhang, Y. Zhang, C. Grezes, P. K. Amiri, K.L. Wang, Appl. Phys. Lett. 110 (2017) 72403.
- [21] Y. Liu, T. Yu, Z. Zhu, H. Zhong, K.M. Khamis, K. Zhu, J. Magn. Magn. Mater. 410 (2016) 123.
- [22] H. Almasi, C.L. Sun, X. Li, T. Newhouse-Illige, C. Bi, K.C. Price, S. Nahar, C. Grezes, Q. Hu, P. Khalili Amiri, K.L. Wang, P.M. Voyles, W.G. Wang, J. Appl. Phys. 121 (2017) 153902.
- [23] M. Cierpiat, K. Grochot, J. Mojsiejuk, J. Wrona, M. Vafae, T. Nan, and W. Skowroński, in 2024 IEEE Int. Magn. Conf. - Short Pap. (INTERMAG Short Pap. (2024)), pp. 1–2.
- [24] S. Isogami, Y. Shiokawa, A. Tsumita, E. Komura, Y. Ishitani, K. Hamanaka, T. Taniguchi, S. Mitani, T. Sasaki, M. Hayashi, Sci. Rep. 11 (2021) 16676.
- [25] T.-Y. Chen, H.-I. Chan, W.-B. Liao, C.-F. Pai, Phys. Rev. Appl. 10 (2018) 44038.
- [26] H. Almasi, D.R. Hickey, T. Newhouse-Illige, M. Xu, M.R. Rosales, S. Nahar, J. T. Held, K.A. Mkhoyan, W.G. Wang, Appl. Phys. Lett. 106 (2015) 182406.
- [27] H. Cheng, J. Chen, S. Peng, B. Zhang, Z. Wang, D. Zhu, K. Shi, S. Eimer, X. Wang, Z. Guo, Y. Xu, D. Xiong, K. Cao, W. Zhao, Adv. Electron. Mater. 6 (2020) 2000271.
- [28] M. Bapna, B. Parks, S. Oberdick, H. Almasi, C. Sun, P. Voyles, W. Wang, S. A. Majetich, J. Magn. Magn. Mater. 483 (2019) 34.
- [29] T. Liu, Y. Zhang, J.W. Cai, H.Y. Pan, Sci. Rep. 4 (2014) 5895.
- [30] T. Yamamoto, T. Ichinose, J. Uzuhashi, T. Nozaki, T. Ohkubo, K. Yakushiji, S. Tamaru, S. Yuasa, Phys. Rev. Appl. 19 (2023) 24020.
- [31] X. Wang, A. Meng, Y. Yao, F. Lin, Y. Bai, X. Ning, B. Li, Y. Zhang, T. Nie, S. Shi, W. Zhao, Nano Lett. 24 (2024) 6931.
- [32] H. Cheng, B. Zhang, Y. Xu, S. Lu, Y. Yao, R. Xiao, K. Cao, Y. Liu, Z. Wang, R. Xu, D. Xiong, Y. Wang, H. Ma, S. Eimer, C. Zhao, W. Zhao, Sci. China Physics, Mech. Astron. 65 (2022) 287511.
- [33] M. Hayashi, J. Kim, M. Yamanouchi, H. Ohno, Phys. Rev. B 89 (2014) 144425.
- [34] B. Fang, X. Zhang, B.S. Zhang, Z.M. Zeng, J.W. Cai, AIP Adv. 5 (2015) 67116.
- [35] H. Almasi, M. Xu, Y. Xu, T. Newhouse-Illige, W.G. Wang, Appl. Phys. Lett. 109 (2016) 32401.
- [36] S. Ikeda, J. Hayakawa, Y. Ashizawa, Y.M. Lee, K. Miura, H. Hasegawa, M. Tsunoda, F. Matsukura, H. Ohno, Appl. Phys. Lett. 93 (2008) 82508.
- [37] T. Yamamoto, T. Ichinose, J. Uzuhashi, T. Nozaki, T. Ohkubo, K. Yakushiji, S. Tamaru, H. Kubota, A. Fukushima, K. Hono, S. Yuasa, J. Phys. D Appl. Phys. 55 (2022) 275003.
- [38] S. Wu, T.L. Jin, F.N. Tan, C.C.I. Ang, H.Y. Poh, G.J. Lim, W.S. Lew, Appl. Phys. Lett. 122 (2023) 122403.
- [39] A. Manchon, S. Zhang, Phys. Rev. B—Condensed Matter Mater. Phys. 78 (2008) 212405.
- [40] J. Huang, C.H. Sim, V.B. Naik, M. Tran, S. Ter Lim, A. Huang, Q.J. Yap, G. Han, J. Magn. Magn. Mater. 401 (2016) 1150.
- [41] T. Yamamoto, T. Nozaki, K. Yakushiji, S. Tamaru, H. Kubota, A. Fukushima, S. Yuasa, Acta Mater. 216 (2021) 117097.
- [42] T. Bonaedy, J.W. Choi, C. Jang, B.-C. Min, J. Chang, J. Phys. D Appl. Phys. 48 (2015) 225002.